Topologically protected parametric wavelength conversion in a valley Hall insulator

Byoung-Uk Sohn,[1] Ju Won Choi, [1] George F. R. Chen, [1] Hongwei Gao, [1] William J. Mitchell, [2] Doris K. T. Ng, [3] and Dawn T. H. Tan[1,3*]

[1]Photonics Devices and System Group, SUTD-MIT International Design Center, Singapore University of Technology and Design, Singapore, 487372, Singapore
[2]NanoFab Facility, Electrical and Computer Engineering Department, University of California Santa Barbara, Santa Barbara, CA 93106, USA
[3]Institute of Microelectronics, A*STAR, 2 Fusionopolis Way, #08-02, Innovis Tower, Singapore 138634, Singapore

* dawn_tan@sutd.edu.sg

Abstract

We investigate nonlinear phenomena in a topological photonic valley Hall insulator using a Kagome system designed to have localized topological boundary state at telecommunications wavelengths. We demonstrate valley Hall topologically protected nonlinear phenomena. Similar transmission properties and parametric wavelength conversion of up to -12dB are experimentally achieved using sub-milliwatt average powers in a zigzag interface without back scattering, compared with a straight interface. Furthermore, we observed a 7dB slow light enhancement in the conversion efficiency near the red edge in the transmission band of the boundary state, demonstrating how slow light induced backscattering may be circumvented by leveraging the topologically protected boundary state. We further experimentally observe a Kerr induced delocalization of the valley Hall topological mode which can be harnessed to control the properties of topological edge states.

Introduction

The discovery of topological insulators in which the boundary state of an electron can propagate without scattering even in the presence of impurities has provided valuable insights into topological photonics [1]. The nontrivial boundary states arise at the interface between two systems with different topological properties. The topology of a system is determined by external parameter spaces that change the system's Hamiltonian such as the wave number of photonic crystal. The topology of the parameter space is characterized by a topological invariant known as the Chern number [2], which is obtained by integrating the Berry curvature over the parameter space. From the perspective of observable physical quantities, the first Hall conductance [3] in a 2D system subjected to an external magnetic field shares the same form as this topological invariant in quantized units of e^2/h . Subsequently, Haldane elucidated the phenomenon of the integer quantum Hall effect in 2D periodic systems without a net magnetic field [4]. The quantized charge transport is connected to Chern numbers, which are applied to the geometry of eigenstates in the parameter space as the Hamiltonian is slowly varied.

Hall conductivity is an odd number quantity under time reversal, allowing for nonzero values in systems where time reversal symmetry is broken. Haldane demonstrated the realization of a time-reversal-breaking system in a 2D periodic setup without a net magnetic field by introducing different hopping phases between nearest neighbours for two basis particles. In the context of the spin Hall effect,[5, 6] the requirement for broken time reversal symmetry, as seen in the quantum Hall effect, is circumvented by considering doubled quantum Hall states that incorporate an additional spin degree of freedom. The spin-orbit interaction, while preserving time reversal symmetry, plays a crucial role in locking the spin to the chiral edge state.

In topological photonics, researchers have successfully incorporated the spin-orbital interaction into metamaterials[7]. However, achieving symmetry for TE and TM polarization requires delicate adjustments. In the Honeycomb structure, the valley degree of freedom (VDF) consists of degenerate states with different crystal momentum, such as K and K'. The VDF has gained attention due to its topological properties exhibiting similarities to the real spin degree of freedom (SDF) observed in 2D monolayers of transition metal dichalcogenide materials like MoS_2[8, 9], as well as bilayer graphene[10-14]. The rotation of the electron wavefunction in the K or K' valleys of the material's band structure results in an additional Berry curvature with opposite signs between the valleys. This resemblance between VDF and SDF gives rise to the emergence of the valley Hall effect (VHE), which is analogous to the spin Hall effect[15]. Similar to the spin-locked (chiral) edge states' immunity to non-magnetic defects at the edges of graphene, the VHE effect leads to valley-locked chiral edge states at the domain walls between different bulk topologies[7, 16-21].

To achieve topological photonic crystals, the VHE can be replicated in photonic crystals with broken inversion symmetry, analogous to MoS_2. This replication results in the suppression of inter-valley scattering and topological protection against various photonic lattice perturbations. The utilization of the VDF in the VHE is more useful and easily accessible in photonics compared to the SDF (polarization). A single (TE or TM) polarization of the photonic modes is sufficient to construct the valley DOF. We can achieve a controllable bandgap that separates different topological phases of propagating light by breaking the inversion symmetry of a unit cell. At the same time, we can implement topological photonic valley insulators using slab waveguides. To date, a variety of applications such as lasing[22], transport[23-26], slow light[27], cavities[28], multiplexers [29] and switches[30-32] have been investigated using protected valley Hall effects.

The valley photonic crystal (VPC) waveguides that support valley-dependent modes are characterized by their robust transmission in the absence of sufficiently strong perturbations or defects breaking the symmetry to cause valley flipping. The light traveling through these waveguides will remain valley locked and will propagate in a unidirectional manner. These types of valley-dependent modes can be enabled by the interface between VPCs with different valley Chern numbers, making VPCs a promising candidate for designing waveguides resistant to sharp bends. Immunity to back-scattering can be used for diverse applications such as directional couplers[33] and lasing[22, 34]; Standard directional couplers need lengths which are much longer than the wavelength of propagating light, whereas a topological directional coupler can be immune to back-scattering in a significantly more compact size. Aside from linear phenomena such as transmission and directional couplers, several papers have theoretically studied nonlinear behaviour in valley Hall topological states of light[35, 36] such as second harmonic generation.

Though topologically protected light propagation has been reported by several groups [7, 18, 21, 23, 24, 34, 37-39], nonlinear optical phenomena in the topological photonic valley Hall insulator has not been investigated to the same extent. In this paper, we experimentally investigate nonlinear phenomena in a topologically protected valley Hall boundary state. We demonstrate topologically protected optical parametric wavelength conversion (OPWC) in a valley Hall photonic crystal. We further observe evidence of slow light enhancement at the edge of the boundary state. Our experimental studies are corroborated by theoretical analyses.

All dielectric topological photonic insulator with Kagome design structure

In this manuscript, the honeycomb unit cell with three circular holes forms the basis used to implement the topological valley insulator (Fig.1(a)). Here, b is the distance between each basis parameter. Based on Kagome symmetry($b = b_0 \equiv \frac{a}{2\sqrt{3}}$), where a is a lattice constant, b may be adjusted by shrinking or expanding from the symmetry,. For the symmetry, the band diagram is shown in Fig. 1(b) as the dashed lines. When inversion symmetry is broken for $b \neq b_0$, the forbidden gap energy is opened as shown as the yellow region in Fig. 1(b), where the stop band exists between 1.524 μm – 1.564 μm for a = 0.49 μm. In this case, Berry curvature in momentum space is calculated by using tight binding theory which considers the dominant hopping amplitude between near basis in intra cell and inter cell as shown in Fig. 1(e) and the topological photonic system implementing valley degrees of freedom with different topology locally near K and K' momentum. The Kagome design has a degenerate point (band inversion) at K and K' on the Brillouin band edge in Brillouin zone as shown as the dashed line in Fig.1(b). The degenerate singular point provides the possibility of a nontrivial topological value when the Kagome symmetry is slightly broken by changing the inter cell hopping amplitude and intra cell hopping amplitude. As shown as the yellow region in Fig. 1 (b), the forbidden band gap opens and the Dirac point disappears, but topology remains near the Dirac point. The Kagome symmetry may be slightly broken by changing b, as shown in Fig. 1(a). Here, perfect Kagome symmetry is defined by satisfying the condition, $b = b_0$.

The symmetry breaking strength determines the forbidden gap width. Stronger symmetry breaking results in a wider gap width. It induces a bandgap at K and K' which are singular points such as Dirac point when symmetry is maintained as shown in Fig. 1 (b), where dashed lines denote the bands for Kagome symmetry and blue and magenta lines denote the bands for slightly broken symmetry ($b = 1.1b_0$). The energy bands in hole momentum space are shown in Fig. 1(c), calculated using tight binding theory for $v < w$ (upper) $v = w$ (lower) , where v and w are the inter-cell and intra-cell hopping amplitude respectively. The mode shape at the K momentum point is shown in Fig.1(d). The left and right figures are for the lower and right bands respectively, whereas the top and bottom figures correspond to $b = 0.9b_0$, and $b = 1.1b_0$ respectively.

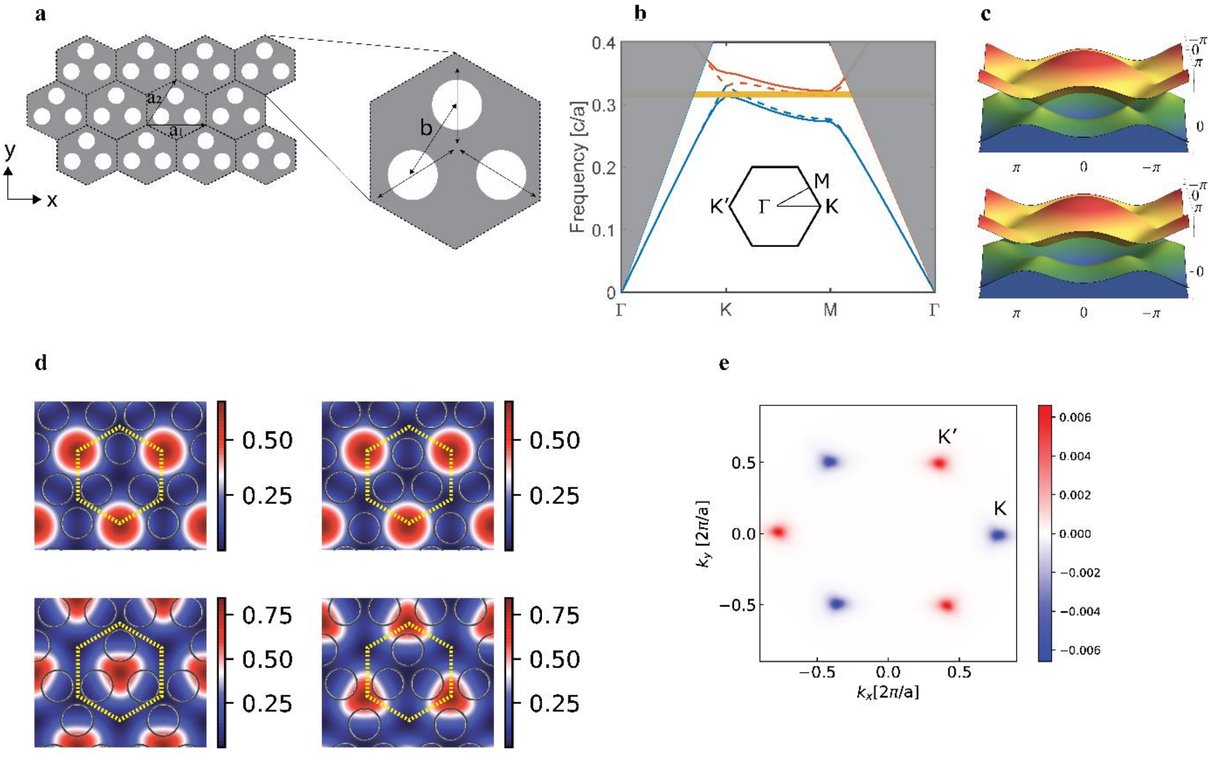

Figure 1. Kagome photonic crystal with non-trivial topology (a) Slightly broken Kagome design with $b = \eta b_0$, where $b_0 = \frac{a}{2\sqrt{3}}$. For $\eta = 1$, Kagome symmetry is satisfied. Here, $\eta = 0.9$. (b) The calculated band diagram for $\eta = 1.1b_0$ and $0.9b_0$. They have the same band diagram distribution. The dashed line corresponds to the band diagram for $\eta = 1$; It has a singular Dirac point for K and K' momenta. When the Kagome symmetry is slightly broken, $\eta \neq 1$ and the band gap opens. The yellow region is the globally forbidden band gap. (c) The energy bands calculated by tight binding theory. The upper and lower figure corresponds to the case with inversion symmetry and inversion symmetry breaking respectively. (d) Calculated modal profiles. The upper two figures and lower two figures correspond to $\eta = 0.9$, and $b = 1.1b_0$ respectively. The left and right figures are modal profiles for the lower and upper bands respectively. The modal profiles have a different shape even though the band diagram for $\eta = 1.1$ and 0.9 is the same. (e) The calculated Berry curvature using the tight binding theory for the lower band. The Berry curvature has different sign and localized for K and K'.

The valley surface-wave photonic crystal's band topology can be characterized using a massive Dirac Hamiltonian of the form, $\mathbf{H} = v_d(\delta k_x \boldsymbol{\sigma}_\mathbf{x} + \delta k_y \boldsymbol{\sigma}_\mathbf{y}) + m\boldsymbol{\sigma}_\mathbf{z}$, where v_d represents the Dirac group velocity of the conical dispersion, $(\delta k_x, \delta k_y)$ represents the momentum deviation from the K(K') point, and $\boldsymbol{\sigma}_\mathbf{x}, \boldsymbol{\sigma}_\mathbf{y}, \boldsymbol{\sigma}_\mathbf{z}$ are the Pauli matrices. The effective mass induced by slight inversion-symmetry breaking is represented by *m*. This Hamiltonian generates a nontrivial valley-dependent Berry curvature, with a distribution sharply centered at the two valleys, as demonstrated in Fig. 1(e). The Berry curvature can be calculated using $\Omega = \boldsymbol{\nabla} k \times \boldsymbol{A}(k)$, where $\boldsymbol{\nabla} k \equiv (\frac{\partial}{\partial \mathrm{k_x}}, \frac{\partial}{\partial \mathrm{k_y}})$ and $\boldsymbol{A}(k)$ is the Berry connection. The Berry connection is defined as $A(k) = -i\langle u_k | \nabla k | u_k \rangle$, where u_k is the normalized Bloch wave function obtained through simulations. The numerical integration of Berry curvature near the K(K') valley results in the valley Chern number $C_{K(K')}$ that takes the values of ±1/2 locally. We note that despite non-zero values of the valley Chern number, the integration of Berry curvature over the entire Brillouin zone is zero due to the system's time-reversal symmetry.

The sign of effective mass, *m* distinguishes two distinct valley topological phases ($b > b_0$ and $b < b_0$), which are separated by a Dirac semimetal phase when $b = b_0$. Consequently, by adjusting b-b_0 from positive to negative, the topological transition of a valley surface-wave photonic crystal can be observed, and the photonic valley pseudospins at the K and K' valleys are reversed at $b = b_0$.

For a valley surface-wave photonic crystal with $b = 1.1b_0$, the near K(K') valley for the lower band results in valley Chern numbers, C_K = -1/2 and $C_{K'}$ = 1/2, which is calculated locally using a surface integral for the Berry curvature in Fig. 1(e) . As b is varied to $b = 0.9b_0$, the valley surface-wave photonic crystal undergoes a topological transition, causing a sign reversal in the corresponding valley Chern numbers. Consequently, for a domain wall separating two different valley surface-wave photonic crystals with opposite half-integer valley Chern numbers, the valley-protected topological charge difference across the interface is quantized ($|C_K| = |C_K - C_{K'}| = 1$), indicating the existence of one chiral edge state per valley propagating along the interface.

In Fig. 2(a), we have created a domain wall between two valley surface-wave photonic crystals, where the upper domain has $b = 0.9b_0$ and the lower domain has $b = 1.1b_0$, resulting in opposite half-integer valley Chern numbers. The band diagram displayed in Fig. 2(b) reveals the existence of valley-polarized topological edge states represented by the red line in the band gap, whose propagation directions are fixed to the K and K' valleys. The black lines in Fig. 2(b) correspond to the bulk states. The grey region in Fig. 2(b) corresponds to the light cone in the cladding for a slab in the *z*-direction. This represents scattered light which may potentially propagate in the cladding, rather than evanescently localized fields.

It may further be observed from Fig. 2 (c) that the mode shape for the boundary state fixed at K and K' is localized to the domain wall.

Using the frequency-momentum k_x relation, one can calculate the effective refractive index of the boundary state as shown in Fig. 2(d). The global band gap region is comprised of grey and yellow areas, where the former is associated with the cladding's light cone and the latter corresponds to a perfectly localized state in the forbidden band gap as calculated in Fig 1(b). Slow light effects could occur for sharply increased refractive indices when the excitation wavelength approaches shorter wavelengths. As k_x approaches $\pm\pi/a$, the group index, n_g is observed to increase more steeply as compared to a waveguide, as shown in Fig. 2(e).

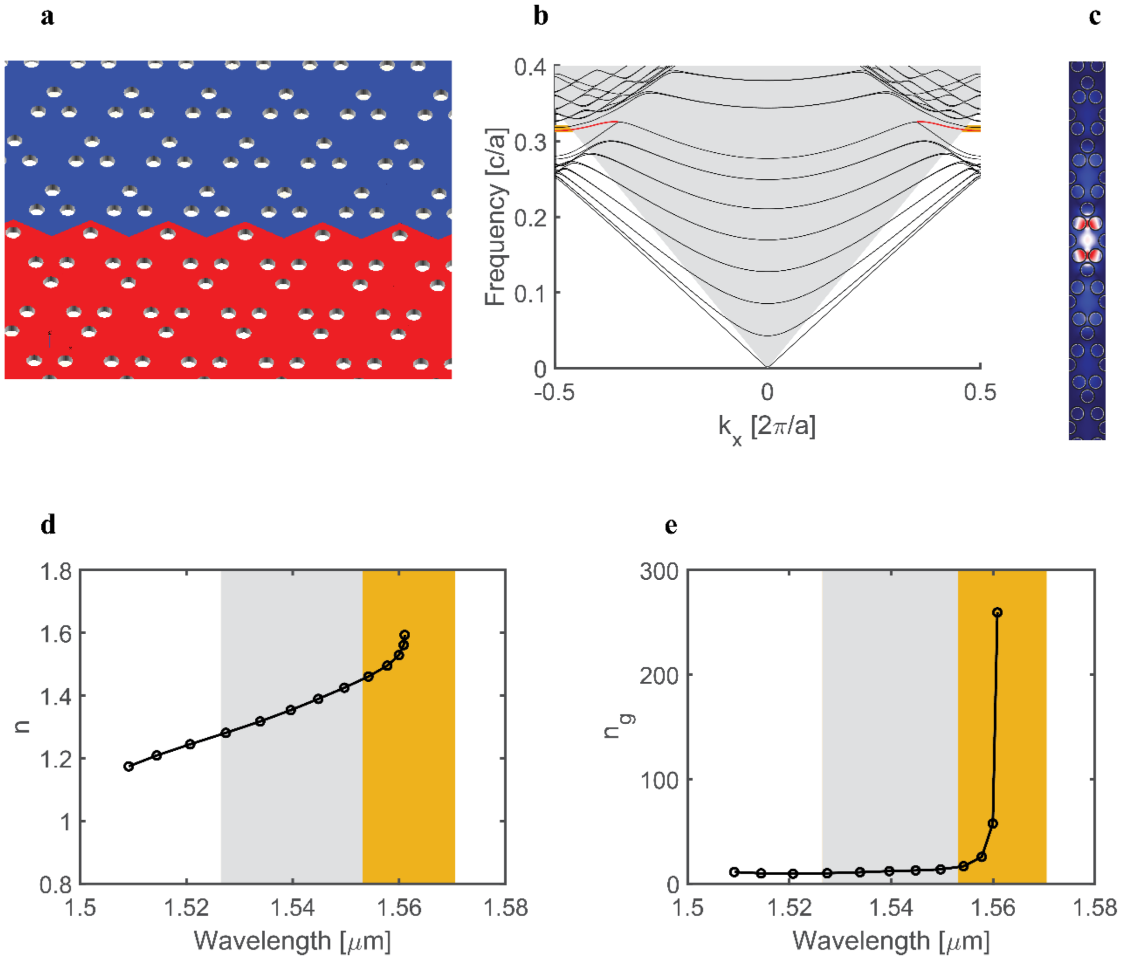

Figure 2. Schematic and properties of a topologically protected domain wall between two different valley photonic crystals. (a) $b = 0.9b_0$ and $b = 1.1b_0$ for the upper and lower domains respectively, with different topologies C = ±1/2 at the K point. The boundary state is generated at the boundary between topology transition of bulk states by bulk-boundary correspondence; the difference $\Delta C^{(k)} = C^{(K)}_{upper} - C^{(K)}_{lower} = +1$. (b) The band diagram is calculated using MEEP for a supercell of 1×14 unit-cells with different topology of C^{K}_{upper} and C^{K}_{lower} as $\frac{1}{2}$ and $-\frac{1}{2}$ respectively, where the red line corresponds to the generated topological boundary state crossing the band gap from upper bulk state to lower bulk state. The grey colored region is the light cone corresponding to the cladding refractive index, where fields are scattered, and not evanescent fields in the cladding. (c) The normalized intensity distribution of the topological boundary state for $k_x = \pi/a$. (d) The effective refractive index of the boundary state retrieved from the relation between frequency and momentum k_x. Regions within the grey and yellow colours are

within the band gap. The grey region is in the light cone for the cladding and the yellow region corresponds to a perfectly localized state. (e) The group index calculated from the effective index using the relation, $n_g = n + \omega \frac{dn}{d\omega}$.

Topological protection conferred by Valley Hall states may be ascertained by investigating transport properties in zigzag paths compared to straight paths. Four sharp edges implemented in a zigzag path (Fig. 3 (d)) will induce large losses in the absence of topologically protected propagation. The loss per sharp edge is measured to be 7.6dB for the conventional photonic waveguide. This is calculated by comparing the signal power for the straight and zigzag conventional photonic waveguides shown in Fig. 4 (g) and Fig. 4 (h) respectively, where it is observed that there is a 30.4dB lower signal level for the zigzag device. Similarly, the loss per sharp edge in the trivial Kagome device may be measured by comparing the straight (Fig. 4 (i)) and zigzag (Fig. 4(j)) configurations. Each bend is characterized to introduce a loss of 2.34dB in the trivial Kagome device. Conversely, the loss at the edge points is almost zero for the topological Kagome photonic based on Fig.3(e); The Kagome photonic device is observed to have negligible losses from the sharp edges. The linear propagation loss of the Kagome photonic device was measured using cutback measurements to be 25dB/cm. To study topologically protected nonlinear phenomena in Valley Hall states, we fabricate devices with a straight and zigzag domain wall to demonstrate robust valley edge transport in the absence of intervalley scattering as shown in Fig. 3 (b). The devices with the straight and zigzag topological interfaces have the same propagation length of 100 µm. The devices are fabricated on 300nm thick ultra-silicon-rich nitride (USRN) We note that USRN is a backend CMOS compatible platform with a high nonlinear figure of merit, and a Kerr nonlinearity of 2.8×10^{-13} cm^2/W [40, 41]. Figure 3 (a) shows a scanning electron micrograph (SEM) of the unit cell making up the fabricated Kagome photonic crystal. Figures 3 (b) and (c) further show scanning electron micrographs of Kagome photonic crystal where the straight and zigzag paths are highlighted in green.

The measured transmission for the Kagome photonic crystals with the straight (blue line) and zigzag (magenta line) interfaces is shown in Fig. 3(e). It is observed that both devices have a similar transmission spectrum, with a band gap located at the wavelength range from 1511nm to 1527nm. To visualize the behaviour of the electromagnetic field propagating through the topological boundary, we studied the $\boldsymbol{E}_y$ field pattern at a wavelength of 1524nm using finite difference time domain simulations, as shown in Fig. 3 (g), where the top figure is for the straight boundary and the bottom figure is for the zigzag boundary. The calculations show the light propagation through the straight and zigzag paths. It is observed that the topological valley edge state can be guided around the zigzag path smoothly without back reflections.

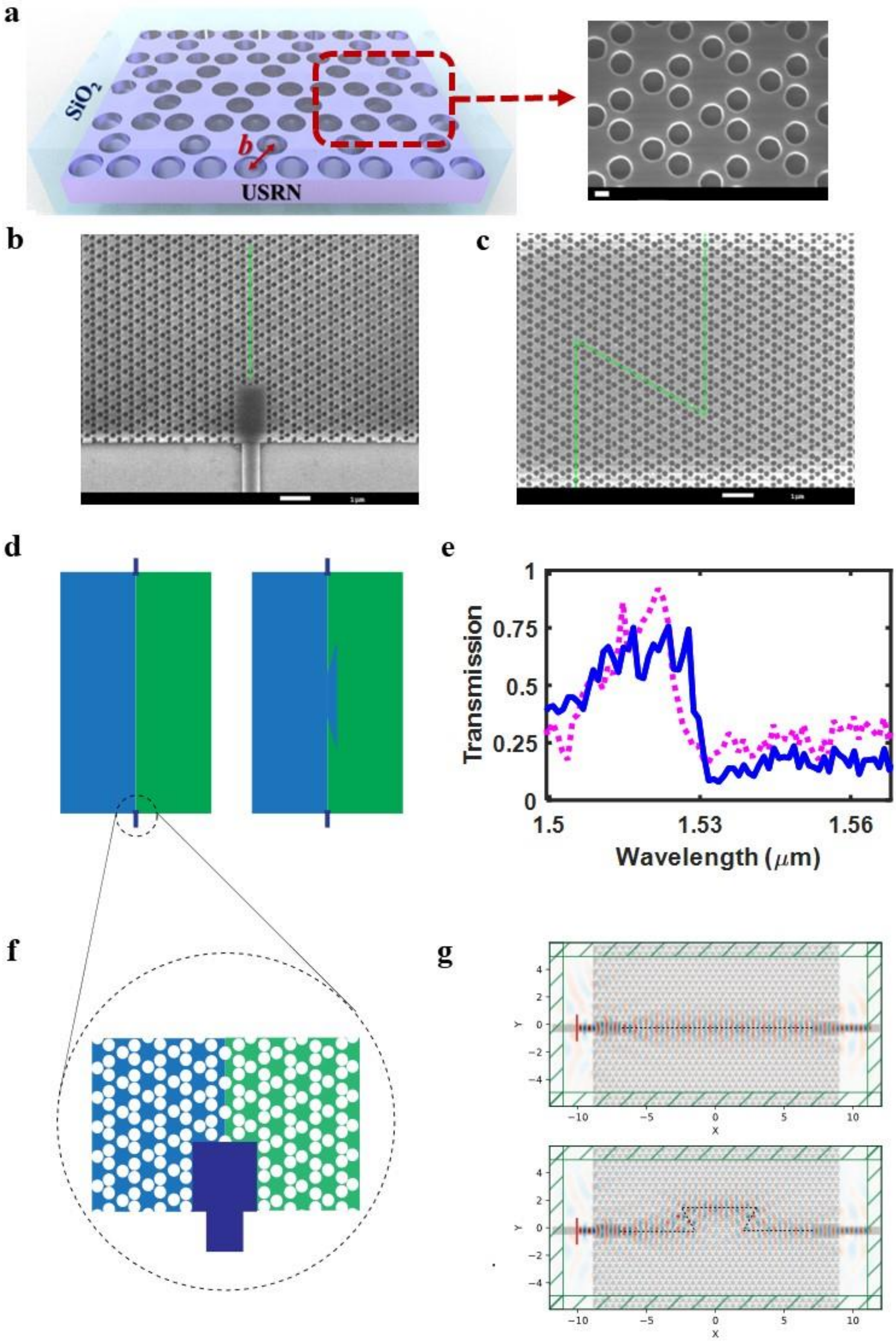
a
SiO2
b
USRN
b
c
d
e
f
g
1
0.75
0.5
0.25
0
1.5
1.53
1.56
Transmission
Wavelength (μm)
Y
X
−10
−5
0
5
10
4
2
0
−2
−4

Figure 3. Transmission at the domain wall with straight and zigzag interfaces. (a) Schematic and SEM of the basis used for the Kagome photonic crystal. The scale bar in the SEM spans 100 nm. The structure is fabricated on a USRN core and SiO_2 cladding. Scanning electron micrograph of the (b) straight and (c) zigzag interfaces. The scale bars span 1µm. (d) Design of the samples showing the straight and zigzag topological boundaries. (e) The measured transmission spectrum for both devices. (f) Schematic of the input and output connectors terminating the devices to maximize transmittance from the waveguide mode to the boundary state by mode matching. (g) Propagation of input fields for straight (upper panel) and zigzag boundary (lower panel) calculated using finite difference time domain simulations. For the purpose of visual representation, green ((b) and (c)) and black (g) dashed lines have been employed in the figures to indicate the location of the domain wall.

Topologically protected parametric wavelength conversion

Parametric processes rely on phase matched nonlinear interactions between a pump and signal in photonic devices [42]. In the case of degenerate four-wave mixing, two pump photons mix with a signal photon to generate an idler photon satisfying the energy conversation ($2\omega_p = \omega_s + \omega_i$) and momentum conversation ($2n(\omega_p)k_p = n(\omega_s)k_s + n(\omega_i)k_i + 2\gamma P$), where ω_p, ω_s, ω_i are frequency of pump beam, signal beam and idler beam respectively, k_p, k_s, k_i are wave number, *n* is the effective refractive index, γ is the nonlinear coefficient, and *P* is the peak power of pump beam. The parametric wavelength conversion efficiency is dependent on the peak power of the pump, how well phase matching is achieved and good temporal overlap (similar group velocities) between the interacting fields. Therefore, any backscattering can have a detrimental effect, as it distorts the dispersion, impacting the conversion efficiency to a greater extent than reduced linear transmission caused by imperfections during fabrication. In this paper, the wavelength of pump, signal and generated idler are closely located. The coherence length $\sim\frac{2\pi}{|\beta_2|\Omega_s^2}$, where β_2, Ω_s is the group velocity dispersion and frequency difference between pump and signal respectively. The coherence length is $4m$, which is much larger than the sample length of $100\mu m$. The walk-off length $\sim T_0/\Delta\beta_1$, where $\Delta\beta_1$ walk-off parameter between signal and idler beam, T_0 is pulse width, is $300\mu m$, which is larger than the sample length.

To demonstrate parametric wavelength conversion, we first perform four-wave mixing experiments in the Kagome photonic crystal with a straight boundary. Figure 4 (a) shows the experimentally measured four-wave mixing spectrum as the peak pump power is increased from 0.45W, 0.55W, 0.7W to 0.88W. It may be observed that the level of the idler (denoted in red) increases as the peak pump power is increased for the pump wavelength. In these four-wave mixing spectra, the pump is located at 1526 nm and the signal located at 1528 nm. Figure 4(b) illustrates the measured conversion efficiency for different input pump wavelengths The blue stars represents a pump wavelength of 1528nm, while the fuchsia circles and black squares correspond to 1526nm and 1524nm, respectively, as depicted in Fig. 4 (c), 4 (d), and 4 (e). The conversion efficiency is observed to be enhanced when the pump wavelength approaches the red edge of the transmission band, as shown in Fig. 4 (b). For a pump wavelength of 1528nm, the conversion efficiency is -18dB at a peak pump power of 0.9W (average power of 90μW). Conversely, for pump wavelengths of 1526nm and 1524nm, the conversion efficiency is -25dB at the same peak power. To derive the conversion efficiency, the average power of the idler beam measured using an optical spectrum analyser (OSA) is converted to peak power by multiplying by the factor, $\frac{1}{R_p T_p}$, where R_p is a repetition rate of pulse and T_p is a pulse width [43, 44]. The conversion efficiency, $CE = 10\ \log_{10}(\gamma_{eff} P_{in} L_{eff})^2$ when phase matching is perfect [45], where $\gamma_{eff} = \frac{2\pi n_2}{\lambda A_{eff}}\left(\frac{n_g}{n_0}\right)^2$, A_{eff} is the effective area of the boundary mode, n_2 is the nonlinear refractive index of core material and P_{in} is the peak power of the pump beam. The measured results indicate that the conversion efficiency scales with $4\log_{10} n_g$. Figure 2 (e) reveals that the group index increases rapidly close to the stopband. The conversion efficiency scales with the fourth power of n_g owing to the slow light effect where the velocity is given by $\frac{c}{n_g}$, thus enhancing the parametric process.

Next, we perform parametric wavelength conversion experiments for the Kagome photonic crystal with a zigzag interface consisting of four 60° bends. Figure 4 (f) shows the four-wave mixing spectrum obtained when the pump and signal are located at 1524 nm and 1528nm respectively. The conversion efficiency for the zigzag boundary type is measured and plotted as the black stars in Fig. 4(b). A conversion efficiency of -15dB is obtained at a peak power of 1.07W, a value which is similar to that of the straight boundary (blue star points in Fig. 4b) although there are slight discrepancies between them because of fabrication bias. The experiments reveal that the nonlinear conversion efficiency is not reduced even when the parametric process takes place in four 60° bends in the zigzag structure. Aside from the comparable conversion efficiency obtained in the straight and zig-zag interfaces, we note that the relatively high conversion efficiencies are obtained in extremely short device lengths and low powers, indicating that nonlinear phenomena can be efficiently harnessed in such structures while simultaneously benefiting from topological protection robust to backscattering. We perform the same OPWC measurements using non-topological devices as shown in Fig. 4(g) and 4(h), for the trivial Kagome photonic device with a straight path and zigzag path respectively, and Fig. 4(i) and 4(j) for the conventional photonic waveguide with straight path and zigzag path respectively. The measured conversion efficiency for the straight, trivial Kagome photonic device (Fig. 4(g)) was -37dB at a peak pump power of 1.38W. This conversion efficiency -15dB lower than that in the topological Kagome device at the same peak power, as shown in Fig. 4(b). We can see the large conversion efficiency enhancement of 22dB in the topological Kagome device. This larger value corresponds to the slow light enhancement brought about by the topological device. The generated idler power for the OPWC measurements done on the zigzag trivial Kagome and zigzag conventional waveguide by the nonlinear four-wave mixing was very low (below the noise level of the OSA) as shown in Fig. 4(h) and 4(j) respectively because of the severe propagation losses in the absence of topological protection.

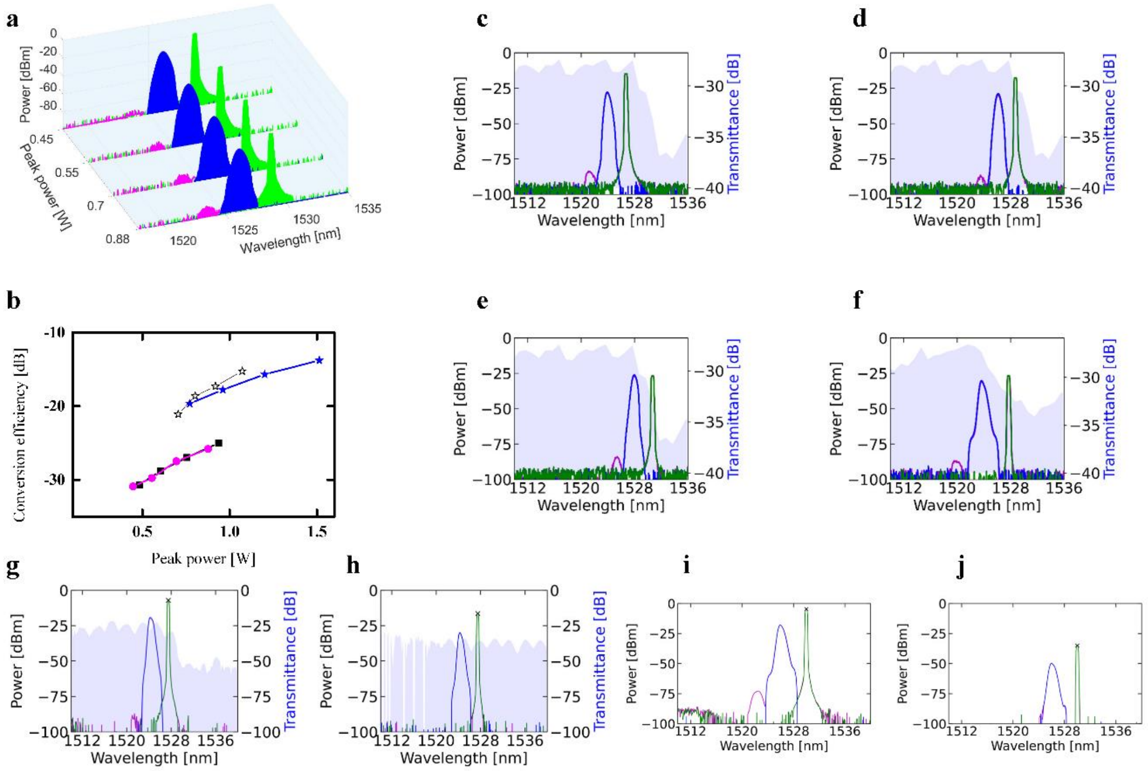

Figure 4. Topologically protected nonlinear OPWC. (a) Experimentally measured OPWC. The input pump, input signal and generated idler are denoted by blue, green and red respectively. (b) Conversion efficiency for straight boundary vs. peak pump power from (c) – (e) (denoted by the fuchsia circles, black squares, and blue stars respectively). The conversion efficiency for the zigzag topological boundary vs. peak pump powers from measurements shown in 4 (g) is denoted as the black stars. OPWC spectra at a pump wavelength of (c) 1524nm, (d) 1526nm and (e) 1528nm. The signal wavelength is 2nm longer than pump wavelengths. The blue background corresponds to the linear transmittance for the sample. (f) OPWC spectrum for the zigzag topological boundary. (g) – (j) represent OPWC experiments performed for non-topological photonic devices. OPWC spectrum for the trivial Kagome photonic device with a (g) straight boundary and (h) zigzag boundary. OPWC spectrum for the conventional photonic waveguide with a (i) straight boundary and (j) zigzag boundary.

Having observed topological protection of OPWC, we further study nonlinear optical phenomena by adopting a longer, 500 μm Kagome photonic crystal. The measured transmission of the sample is shown in Fig. 5 (a). In this device, we observe power dependent self-phase modulation as shown in Fig. 5 (c). In addition, power dependent transmission measurements reveal that the transmitted power deviates from a linear relationship at higher powers as shown in Fig. 5b. Our analysis reveals that this deviation is due to a Kerr perturbation to the region where light is guided along the topological boundary and induces a change in the chiral edge states. The effect of Kerr nonlinearity on transmission may be simulated in the simplified reduced device size with the straight boundary in Fig. 5 (d) – (f). The transmitted spectrum is changed by the strength of the nonlinear coefficient containing input peak power and conventional third order of susceptibility, $\chi^{(3)} \equiv \chi^{(3)}|E_{in}|^2$ as shown in Fig. 5 (d). For the highest nonlinearity of $\chi^{(3)} = 0.79$, the field is observed to no longer be guided along the topological interface, as shown in Fig. 5 (f). For a smaller extent of nonlinear perturbation ($\chi^{(3)} = 0.01$) shown in Fig. 5e, the field continues to be well guided though compared to the non-perturbed case, the transmitted light is reduced. Thus, when the nonlinear Kerr effect with high peak power perturbs the topological boundary state, the output power cannot increase linearly with input power. Rather, the output power starts to saturate at a threshold input peak power.

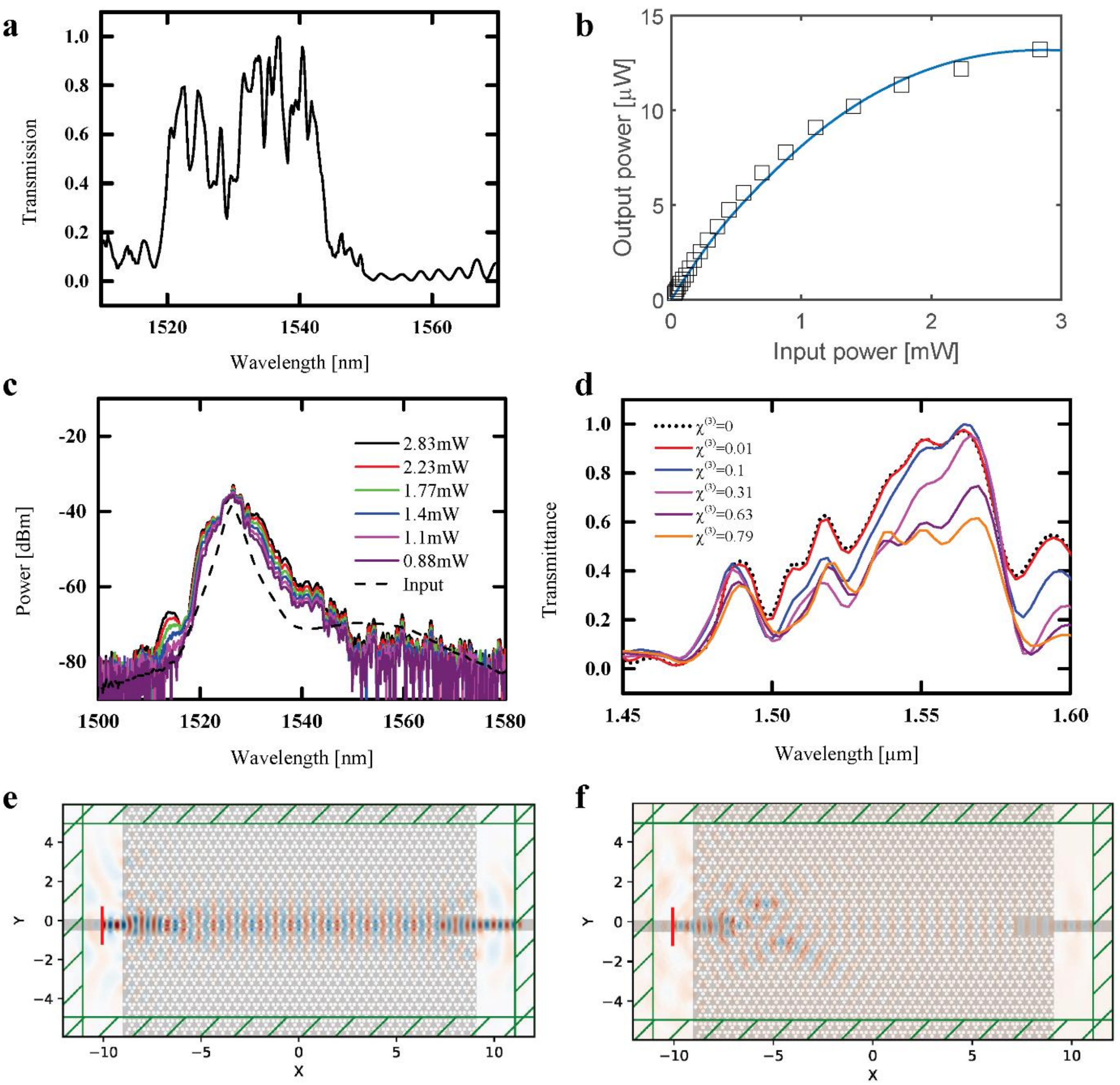

Figure 5. Experimental characterization of a 500μm Kagome photonic crystal with a straight interface. (a) Measured transmission spectrum. (b) Output power as a function of input power, where square points are measured, and the line represents the theoretical calculation using Meep. (c) Output spectrum as a function of input power showing self-phase modulation. (d) The theoretically calculated transmittance using Meep as a function of $\chi^{(3)}$. Numerically calculated field propagation for (e) $\chi^{(3)} = 0.01$ and (f) $\chi^{(3)} = 0.79$.

Discussion

In our study, we performed OPWC in a topological photonic crystal, which serves as a crucial boundary for assessing the propagation characteristics of nonlinear optics. Specifically, we focused on a propagation path characterized by the presence of four sharp edges, aiming to gain insight into its behaviour by analysing the experimental data, we found that the idler conversion efficiency exhibited remarkable similarities between the straight and zigzag shapes. Notably, these similarities were observed at the exact same pump wavelength position, which happened to coincide with the edge of the transmission bands. This intriguing discovery implies that there is no discernible distinction in the group index, a fundamental parameter related to the propagation properties, between the straight and zigzag configurations. The topological photonic device is designed to implement the valley Hall effect at telecommunications wavelengths using the highly nonlinear ultra-silicon-rich nitride material. OPWC is experimentally demonstrated, and a slow light enhancement of 7dB for approximate 1W of peak power when the spectrum of the pump approaches the red edge of the forbidden band is achieved. Topologically protected OPWC is inherently immune to backscattering, thus allowing similar extents of conversion efficiency to be observed in both the straight and zigzag configurations.

It has previously been reported that optical nonlinearities can be used to modify or control topological modes. In laser written silica waveguides, megawatt peak powers induced a sufficiently large increase in the refractive index, driving the lattice into the topologically nontrivial regime [46, 47]. Kerr induced delocalization of topological states was demonstrated at few watt peak powers in a Su Schrieffer Heeger topological waveguide [48] and nonlinear perturbations to valley-locked chiral edge states have not yet been reported in valley Hall photonic crystals. In this manuscript, evidence of optical nonlinearities impacting the valley Hall topological mode was observed from power dependent transmission measurements, which showed the transmitted light deviating from a linear profile. Numerical simulations confirm the impact of varying extents of nonlinearity on topological mode propagation.

We further observed slow light effects in the valley Hall photonic crystal, from an enhanced conversion efficiency closer to the edge of the stopband. The slow light regime for electromagnetic field materials with elevated group indices is a pertinent topic as it may be harnessed for the implementation of optical storage systems as a precursor to logical transformation of information written on quantum systems of electromagnetic fields. When electromagnetic fields encounter a sudden change in material refractive index, they will undergo Fresnel refraction. A marginal change in refractive index is a necessary condition to reduce loss or distortion of the optical fields. It could be relatively easy to satisfy this requirement for generation of the topological boundary state; This topological boundary state is usually generated in the middle of the band gap as a zero mode. When we tune the band gap by breaking inversion symmetry in the Kagome system, the slope of effective refractive index is changed but the effective index itself is unchanged, especially near the middle of band gap. When the optical field encounters the slow light regime, the field amplitude, A increases via a compacted field near the change of group index, approximately given by $A \sim A_0 n_g$. Slow light propagating in media also means that the interaction time is increased between the electric field and material, giving rise to enhanced light matter interaction. Interaction between photons propagating in materials may be increased through this increased interaction time. This nonlinear behaviour is important for all-optical control of weak fields down to the photon level. However, the increased interaction time could also pose a negative effect. Slowly varying environmental fluctuations such as thermal vibrations with a characteristic time scale of $\sim 1/\omega_v$, where ω_v is frequency of phonon, or spatial defects could impact the integrity of quantum information carried in the fields, thus causing erasure of information. It may therefore be stated that noise or unintended defects have a more critical, detrimental effect on a quantum system. Thus, it should be emphasized that the topological property is more important in the slow light system. Topologically protected nonlinear phenomena in the slow light regime is an important function. However, topological protection does not apply to other features of the device: We cannot avoid any internal degree of freedom nor is the vertical thickness dimension topologically protected (z-direction in Fig. 1a). In addition, loss may be induced from any degree of freedom that is topologically unprotected. Indeed, a recent study confirmed that valley Hall topological photonic devices do not provide topological protection against fabrication induced backscattering[49].

We note that tailoring of the group index profile may be achieved by changing the width of the band gap. A wider/more open band gap increases the refractive index slope corresponding to the group index, even though the position is fixed on the Brillouin boundary for the super cell, $k_x = \pm\pi/a$. Because the tuning cannot alter the refractive index near the Brillouin boundary, we can freely change the group velocity without any Fresnel refraction. Furthermore, in our design, the band gap is small, and the topological boundary state is implemented in the narrow band gap. Consequently, the state is not as well localized in the system compared to one with a wider gap. However, the topological boundary state is almost identical to that of the flat band. In the future, this system could provide a window into investigating dynamics of light propagation in flat topological boundaries.

Lastly, we note that parametric conversion in 1D topological photonic structures described by the phenomenological Su-Schrieffer-Heeger model was recently demonstrated [48]. A boundary waveguide where chiral symmetry is preserved, strongly localizes the topological mode and facilitates its interaction with the Kerr nonlinearity. It should be noted that the topological protection for nonlinear conversion conferred by the valley Hall insulator demonstrated in this work is distinct from that of the SSH waveguide. The valley Hall topological waveguide in this work provides topological protection of the propagating light and nonlinear conversion against backscattering which can be induced for example through the presence of sharp bends. Conversely, topological waveguides described by the SSH model provide topological immunity only to fluctuations in the coupling constants within the array which can be induced by fabrication imperfections [50, 51]. Consequently, the valley Hall insulator here has some distinct advantageous features pertaining to topological protection, as well as the possibility of slow-light enhancement in the nonlinear conversion process.

In conclusion, we have demonstrated topologically protected OPWC in a valley Hall photonic crystal. The conversion efficiency benefits from the high optical nonlinearity of the core media (USRN), allowing low power operation (sub-milliwatt) while simultaneously adopting topologically protected traits conferred by effective time reversal symmetry breaking in the Kagome photonic crystal. We observed similar transmission spectra and nonlinear conversion efficiencies in both the straight interface and the zigzag interface with four 60 degree bends, as well as evidence of Kerr induced perturbation in the topological mode. Slow light effects observed on the band edge of the Kagome photonic crystal provide further nonlinear enhancement. The CMOS-compatibility and efficient, low power (sub-milliwatt) operation at telecommunications wavelengths may have profound implications on topologically protected light sources and packet switching of high-speed data, potentially also serving as a platform for nonlinear tuning of topological devices.

Materials and Methods

Fabrication

Fabrication is performed on a 300nm USRN film. The USRN film is deposited on a 5 µm thermal oxide on silicon substrate using chemical vapor deposition at a low temperature of 250 °C. Next, electron beam lithography is used to pattern the devices. Inductively coupled plasma etching is performed to define the patterned structures. Finally, 2µm of SiO_2 cladding is deposited using plasma enhanced chemical vapor deposition. Inverse tapers are patterned to facilitate the coupling of light from optical fiber into the samples. The coupling loss at each waveguide-fiber interface is 6 dB.

Four-wave mixing measurements

A 5ps pulsed pump at a repetition rate of 20MHz and a continuous-wave signal are first filtered respectively using band pass filters with -90dB rejection to minimize back-reflected light. The pump and signal are subsequently combined using a 3dB coupler before being coupled into the topological devices using tapered lensed fibers. The optical field at the output is coupled into an optical spectrum analyzer using a tapered lensed fiber in order to characterize the four-wave mixing spectrum.

Numerical calculations

MEEP, an open source software based on python is utilized for numerical calculations and simulations. The band diagram for the topological design is calculated using the mode solver for a supercell of 1×14 unit-cells and the transmission is calculated using finite difference time domain calculations.

Acknowledgments

Funding from the Ministry of Education ACRF Tier 2 Grant (T2EP50121-0019), A*STAR MTC Grant (M21K2c0119), Quantum Engineering Programme Grant (NRF2022-QEP2-01-P08) and A*STAR (C220415015) is gratefully acknowledged. The authors acknowledge processing and facilities under the National Research Foundation, Prime Minister's Office, Singapore, under its Medium Sized Centre Program, the Singapore University of Technology and Design, the UCSB Nanofabrication Facility, an open access laboratory, and the Agency for Science, Technology and Research.

Data Availability Statement

Data from this study is available from the corresponding author upon reasonable request.

Conflict of interest

The authors declare no conflict of interest.

REFERENCES

[1] L. Lu, J.D. Joannopoulos, M. Soljačić, *Nat. Photonics*, 8 **2014**, 821-829.
[2] D. Sheng, Z. Weng, L. Sheng, F. Haldane, *Phys. Rev. Lett.*, 97 **2006**, 036808.
[3] Y. Zhang, Y.-W. Tan, H.L. Stormer, P. Kim, *Nature*, 438 **2005**, 201-204.
[4] F.D.M. Haldane, *Phys. Rev. Lett.*, 61 **1988**, 2015.
[5] A. Hoffmann, *IEEE transactions on magnetics*, 49 **2013**, 5172-5193.
[6] J. Sinova, D. Culcer, Q. Niu, N. Sinitsyn, T. Jungwirth, A.H. MacDonald, *Phys. Rev. Lett.*, 92 **2004**, 126603.
[7] J.-W. Dong, X.-D. Chen, H. Zhu, Y. Wang, X. Zhang, *Nature materials*, 16 **2017**, 298-302.
[8] K.F. Mak, K.L. McGill, J. Park, P.L. McEuen, *Science*, 344 **2014**, 1489-1492.
[9] J. Lee, K.F. Mak, J. Shan, *Nat. Nanotechnol.*, 11 **2016**, 421-425.
[10] Y. Kim, K. Choi, J. Ihm, H. Jin, *Phy. Rev. B*, 89 **2014**, 085429.
[11] Y. Zhang, T.-T. Tang, C. Girit, Z. Hao, M.C. Martin, A. Zettl, M.F. Crommie, Y.R. Shen, F. Wang, *Nature*, 459 **2009**, 820-823.
[12] J. Li, K. Wang, K.J. McFaul, Z. Zern, Y. Ren, K. Watanabe, T. Taniguchi, Z. Qiao, J. Zhu, *Nat. Nanotechnol.*, 11 **2016**, 1060-1065.
[13] L. Ju, Z. Shi, N. Nair, Y. Lv, C. Jin, J. Velasco Jr, C. Ojeda-Aristizabal, H.A. Bechtel, M.C. Martin, A. Zettl, *Nature*, 520 **2015**, 650-655.
[14] X. Xu, W. Yao, D. Xiao, T.F. Heinz, *Nat. Phys.*, 10 **2014**, 343-350.
[15] C.L. Kane, E.J. Mele, *Phys. Rev. Lett.*, 95 **2005**, 226801.
[16] A.B. Khanikaev, S. Hossein Mousavi, W.-K. Tse, M. Kargarian, A.H. MacDonald, G. Shvets, *Nature materials*, 12 **2013**, 233-239.
[17] Q. Tang, M.R. Belić, Y.Q. Zhang, Y.P. Zhang, Y.D. Li, *Nonlinear Dynamics*, 108 **2022**, 1573-1583.
[18] J.-W. Liu, F.-L. Shi, X.-T. He, G.-J. Tang, W.-J. Chen, X.-D. Chen, J.-W. Dong, *Adv. Phys-X*, 6 **2021**, 1905546.
[19] T. Ma, G. Shvets, *New Journal of Physics*, 18 **2016**, 025012.
[20] S. Barik, A. Karasahin, C. Flower, T. Cai, H. Miyake, W. DeGottardi, M. Hafezi, E. Waks, *Science*, 359 **2018**, 666-668.
[21] W.-M. Deng, X.-D. Chen, W.-J. Chen, F.-L. Zhao, J.-W. Dong, *Nanophotonics*, 8 **2019**, 833-840.
[22] Y. Gong, S. Wong, A.J. Bennett, D.L. Huffaker, S.S. Oh, *Acs Photonics*, 7 **2020**, 2089-2097.
[23] Z. Gao, Z. Yang, F. Gao, H. Xue, Y. Yang, J. Dong, B. Zhang, *Phy. Rev. B*, 96 **2017**, 201402.
[24] F. Gao, H. Xue, Z. Yang, K. Lai, Y. Yu, X. Lin, Y. Chong, G. Shvets, B. Zhang, *Nat. Phys.*, 14 **2018**, 140-144.
[25] T. Ma, A.B. Khanikaev, S.H. Mousavi, G. Shvets, *Phys. Rev. Lett.*, 114 **2015**, 127401.
[26] P. Liu, H. Zeng, D.A. Czaplewski, N.P. Stern, *ACS Photonics*, 9 **2022**, 922-928.
[27] H. Yoshimi, T. Yamaguchi, Y. Ota, Y. Arakawa, S. Iwamoto, *Opt. Lett.*, 45 **2020**, 2648-2651.
[28] Y. Li, Y. Yu, F. Liu, B. Zhang, G. Shvets, *Phys. Rev. Lett.*, 125 **2020**, 213902.
[29] Y. Xu, W. Zhou, K. Chen, X. Huang, *Opt. Laser Technol.*, 155 **2022**, 108422.
[30] H. Wang, G. Tang, Y. He, Z. Wang, X. Li, L. Sun, Y. Zhang, L. Yuan, J. Dong, Y. Su, *Light Sci. Appl.*, 11 **2022**, 292.
[31] Z. Qi, G. Hu, C. Deng, H. Sun, Y. Sun, Y. Li, B. Liu, Y. Bai, S. Chen, Y. Cui, *Nanophotonics*, 11 **2022**, 4273-4285.
[32] K. Guo, Q. Xue, F. Chen, K. Zhou, S. Liu, Z. Guo, *J. Appl. Phys.*, 130 **2021**, 203105.
[33] X.-T. He, E.-T. Liang, J.-J. Yuan, H.-Y. Qiu, X.-D. Chen, F.-L. Zhao, J.-W. Dong, *Nat. Commun.*, 10 **2019**, 872.
[34] H. Zhong, Y. Li, D. Song, Y.V. Kartashov, Y. Zhang, Y. Zhang, Z. Chen, *Laser Photonics Rev.*, 14 **2020**, 2000001.
[35] D.A. Smirnova, L.A. Smirnov, E.O. Smolina, D.G. Angelakis, D. Leykam, *Phys. Rev. Res.*, 3 **2021**, 043027.
[36] Z. Lan, J.W. You, Q. Ren, E. Wei, N.C. Panoiu, *Phys. Rev. A*, 103 **2021**, L041502.
[37] H. Xue, Y. Yang, B. Zhang, *Adv. photonics*, 2 **2021**, 2100013.

[38] S.A.H. Gangaraj, G.W. Hanson, *IEEE Antennas and Wireless Propagation Letters*, 16 **2016**, 449-452.
[39] Y. Tian, Y. Zhang, Y. Li, M.R. Belić, *Frontiers of Physics*, 17 **2022**, 53503.
[40] D.T. Tan, D. Ng, J. Choi, E. Sahin, B.-U. Sohn, G. Chen, P. Xing, H. Gao, Y. Cao, *Adv. Phys-X*, 6 **2021**, 1905544.
[41] B.-U. Sohn, J.W. Choi, D.K. Ng, D.T. Tan, *Sci. Rep.*, 9 **2019**, 10364.
[42] G.P. Agrawal, Nonlinear fiber optics, 2nd ed., Academic Press1995.
[43] K.-Y. Wang, A.C. Foster, *J. Opt.*, 17 **2015**, 094012.
[44] X. Liu, R.M. Osgood, Y.A. Vlasov, W.M. Green, *Nat. Photonics*, 4 **2010**, 557-560.
[45] J.W. Choi, B.-U. Sohn, E. Sahin, G.F. Chen, P. Xing, D.K. Ng, B.J. Eggleton, D.T. Tan, *Nanophotonics*, 10 **2021**, 3507-3518.
[46] L.J. Maczewsky, M. Heinrich, M. Kremer, S.K. Ivanov, M. Ehrhardt, F. Martinez, Y.V. Kartashov, V.V. Konotop, L. Torner, D. Bauer, *Science*, 370 **2020**, 701-704.
[47] S. Xia, D. Kaltsas, D. Song, I. Komis, J. Xu, A. Szameit, H. Buljan, K.G. Makris, Z. Chen, *Science*, 372 **2021**, 72-76.
[48] B.-U. Sohn, Y.-X. Huang, J.W. Choi, G.F. Chen, D.K. Ng, S.A. Yang, D.T. Tan, *Nat. Commun.*, 13 **2022**, 7218.
[49] C.A. Rosiek, G. Arregui, A. Vladimirova, M. Albrechtsen, B. Vosoughi Lahijani, R.E. Christiansen, S. Stobbe, *Nat. Photonics*, **2023**, 1-7.
[50] A. Blanco-Redondo, B. Bell, D. Oren, B.J. Eggleton, M. Segev, *Science*, 362 **2018**, 568-571.
[51] Z. Zhang, M.H. Teimourpour, J. Arkinstall, M. Pan, P. Miao, H. Schomerus, R. El-Ganainy, L. Feng, *Laser Photonics Rev.*, 13 **2019**, 1800202.